



1 **New observations of the distribution, morphology, and dissolution dynamics of**
2 **cryogenic gypsum in the Arctic Ocean**

3

4 **Jutta E. Wollenburg¹, Morten Iversen², Christian Katlein¹, Thomas Krumpen¹, Marcel**
5 **Nicolaus¹, Giulia Castellani¹, Ilka Peeken¹, Hauke Flores¹**

6 ¹Alfred-Wegener-Institut Helmholtz-Zentrum für Polar- und Meeresforschung, D-27570,
7 Bremerhaven, Germany

8 ²MARUM and University of Bremen, D-27359, Bremen, Germany

9 ¹Corresponding author and requests for materials should be addressed to J.E.W. (email:
10 Jutta.Wollenburg@awi.de)

11



12 **Abstract**

13 To date observations on a single location indicate that cryogenic gypsum ($\text{Ca}[\text{SO}_4] \cdot 2\text{H}_2\text{O}$) may
14 constitute an efficient but hitherto overlooked ballasting mineral enhancing the efficiency of
15 the biological carbon pump in the Arctic Ocean. In June-July 2017 we sampled cryogenic
16 gypsum under pack-ice in the Nansen Basin north of Svalbard using a plankton net mounted
17 on a Remotely Operated Vehicle (ROVnet). Cryogenic gypsum crystals were present at all
18 sampled stations, which suggested a persisting cryogenic gypsum release from melting sea ice
19 throughout the investigated area. This was supported by a sea ice backtracking model that
20 indicated that gypsum release was not related to a specific region of sea ice formation. The
21 observed cryogenic gypsum crystals exhibited a large variability in morphology and size, with
22 the largest crystals exceeding a length of 1 cm. Preservation, temperature and pressure
23 laboratory studies revealed that gypsum dissolution rates accelerated with increasing
24 temperature and pressure, ranging from 6% d^{-1} by mass in Polar Surface Water ($-0.5\text{ }^\circ\text{C}$) to
25 81% d^{-1} by mass in Atlantic Water ($2.5\text{ }^\circ\text{C}$ at 65 bar). When testing the preservation of gypsum
26 in Formaldehyde-fixed samples we observed immediate dissolution. Dissolution at warmer
27 temperatures and through inappropriate preservation media may thus explain why cryogenic
28 gypsum was not observed in scientific samples previously. Direct measurements of gypsum
29 crystal sinking velocities ranged between 200 and 7000 m d^{-1} indicated that gypsum-loaded
30 marine aggregates could rapidly sink from the surface to abyssal depths, supporting the
31 hypothesised potential as a ballasting mineral in the Arctic Ocean.

32

33 **Keywords:**

34 Cryogenic gypsum, Arctic Ocean, mineral ballasting, biological carbon pump, sea ice.

35



36 **1 Introduction**

37 Climate change in the Arctic Ocean has led to a drastic reduction of summer sea ice extent as
38 well as to a significant thinning of the sea ice (Kwok, 2018; Kwok and Rothrock, 2009). Sea
39 ice strength has reduced, and increased deformation and fractionation result in a progressively
40 increasing sea ice drift speed (Docquier et al., 2017) and sea ice export. Over the past decades
41 the ice export via the Fram Strait alone has increased by 6% and 11% per decade as annual
42 mean, and during the productive spring and summer period, respectively (Smedsrud et al.,
43 2017). An increasing amount of sea ice produced in the East Siberian and Laptev Sea melts
44 over the adjacent continental slopes or in the central Arctic Ocean (Krumpfen et al., 2019).
45 Overall, the Arctic Ocean sea ice cover has shifted to a predominantly seasonal ice cover.
46 However, although the majority of sea ice diminishes during late summer, the amount of sea
47 ice produced in autumn to winter progressively increases (Kwok, 2018).

48 Large-scale transformations in the seasonal sea ice cover impact the physical, chemical and
49 biological dynamics of the sea ice-ocean system. However, especially the interactions of
50 physical-chemical processes within the sea ice and pelagic to benthic biological processes
51 have only received little attention. Of particular importance are poorly soluble minerals
52 precipitated within the brine channels of sea ice which, once released, may ballast organic
53 material sinking to the sea-floor. The changing icescape with more leads and the thinner
54 Arctic sea ice allows increasing light penetration into the under-ice surface water (Katllein et
55 al., 2015; Nicolaus et al., 2013; Nicolaus et al., 2012), supporting fast-growing and often
56 massive under-ice phytoplankton blooms (Arrigo et al., 2012; Arrigo et al., 2014; Assmy et
57 al., 2017). A recent study reported on a sudden export event of an under-ice bloom of the
58 ‘unsinkable alga’ *Phaeocystis*, caused by the ballasting effect of cryogenic gypsum released
59 from melting sea ice (Wollenburg et al., 2018a). This single event was the first and only
60 report of cryogenic gypsum release in the Arctic Ocean. Moreover, this sea ice precipitation
61 of cryogenic gypsum has never been recorded in Arctic sediments, sediment traps or other
62 field studies.

63 When sea ice forms, the concentrations of dissolved ions in brine increase, and depending on
64 the temperature of sea ice, a series of minerals (ikaite, mirabilite, hydrohalite, gypsum,
65 hydrohalite, sylvite, MgCl₂, Antarcticite) precipitate (Butler, 2016; Butler and Kennedy, 2015;
66 Geilfus et al., 2013; Golden et al., 1998; Wollenburg et al., 2018a). Once released into the
67 ocean, gypsum seems to be the most stable of the cryogenic precipitates (Butler et al., 2017;



68 Strunz and Nickel, 2001). Sea ice derived cryogenic gypsum was firstly described by Geilfus
69 et al. (Geilfus et al., 2013), in a comprehensive work on the chemical, physical, and
70 mineralogical aspects of its precipitation in experimental and natural sea ice off Greenland.
71 According to FREZCHEM, a chemical–thermodynamic model that was developed to quantify
72 aqueous electrolyte properties at sub-zero temperatures, cryogenic gypsum can precipitate at
73 temperatures below $-18\text{ }^{\circ}\text{C}$, and within a small temperature window between -6.5 and -8.5
74 $^{\circ}\text{C}$ (Geilfus et al., 2013; Marion et al., 2010; Wollenburg et al., 2018a). However,
75 measurements on the stoichiometric solubility products showed that gypsum dynamics in ice–
76 brine equilibrium systems strongly depend on the solubility and precipitation of hydrohalite
77 and mirabilite (Butler, 2016; Butler et al., 2017). So far gypsum precipitation in experimental
78 setups were only observed at temperatures between -7.1 and $-8.2\text{ }^{\circ}\text{C}$, and not in the lower
79 temperature range (Butler, 2016; Butler et al., 2017). Moreover, as Arctic sea ice rarely
80 reaches temperatures lower than $-18\text{ }^{\circ}\text{C}$, cryogenic gypsum is more likely precipitated within
81 the higher temperature window in the Arctic Ocean (Wollenburg et al., 2018a).

82 A model applied to understand the gypsum release event of 2015 showed that the ice flow
83 was to warm when it started to form and identified December to February as the most likely
84 time span for gypsum precipitation (Wollenburg et al., 2018a). Due to the absence of a
85 downward brine flux in this advanced phase of sea ice formation, gypsum crystals likely
86 remain trapped in the ice until spring. In the absence of sufficient field observations gypsum
87 release from sea ice is expected to peak at the beginning of the melting season, when sea ice
88 warms to temperatures above $-5\text{ }^{\circ}\text{C}$. This temperature marks the transition in the fluid
89 transport capacities of sea ice allowing brine water and included crystals to be released into
90 the water column (Golden et al., 1998). However, in lack of any extensive, best year-round
91 field studies our knowledge depends on models, kinetics and two single field observations
92 (Geilfus et al., 2013; Wollenburg et al., 2018a). There are no studies on sea ice-derived
93 cryogenic gypsum crystal morphologies and its stability in seawater. It is unclear whether
94 gypsum just precipitates during the assumed peak in December to February or whether it
95 continues to grow from remaining brines during sea ice drift. We therefore need more studies
96 on the formation and release of cryogenic gypsum to assess its impact on biogeochemistry in
97 the Arctic and sub-Arctic.

98 In this study, we systematically investigated the occurrence of cryogenic gypsum release from
99 sea ice in spring 2017 with special emphasis on the overall appearance of the crystals.
100 Varieties of cryogenic gypsum crystal morphologies are described and illustrated. The



101 sampled gypsum crystals were further subjected to various laboratory experiments. Hereby,
102 the dissolution behaviour over typical depth- and temperature ranges of the Arctic water
103 column, in Formaldehyde solution typically used in biological sampling were investigated and
104 the sinking speed of gypsum crystal measured. These experiments were conducted to answer
105 the question, why cryogenic gypsum has not previously been observed in field studies and if it
106 qualifies as ballast mineral.

107

108

109 **2 Material and Methods**

110 **2.1 Gypsum sampling with the ROVnet and on-board treatment**

111 RV *Polarstern* expedition PS 106 (June-July 2017) in the early melting season gave the
112 opportunity to systematically study the occurrence of cryogenic gypsum release and the
113 overall appearance of crystals in the area north of the Svalbard and on the Barents Sea shelf
114 (Fig. 1A; Table 1).

115 Cryogenic gypsum was sampled from the upper 10 m of the under-ice water at four stations
116 distributed throughout the expedition area (Fig. 1A; Table 1). The first part of the expedition
117 (PS106/1) consisted of a drift study to the north of Svalbard, during which the vessel was
118 anchored to an ice floe (station 32). This ice floe was revisited 6 weeks later at the end of the
119 expedition (PS106/2) (station 80). During the second part of the expedition (PS106/2),
120 cryogenic gypsum was collected over the western Barents Sea (station 45) and in the Nansen
121 Basin to the north-east of Svalbard (station 66). Gypsum crystals were sampled with a
122 plankton net mounted on a remotely operated vehicle (ROVnet). The ROVnet consists of a
123 Polycarbonate frame with an opening of 40 cm by 60 cm, to which a zooplankton net with a
124 mesh size of 500 μm was attached (Flores, 2018). For gypsum sampling, a handmade nylon
125 net with an opening of 10 cm by 15 cm and a mesh size of 30 μm was mounted in the
126 zooplankton net opening. The concentrated particulate material of the small nylon net was
127 collected in a 2 L polyethylene bottle attached to the cod end of the net. A gauze-covered
128 window in the cod-end bottle allowed seawater to drain off. Both nets were mounted on the
129 aft end of a M500 (Ocean Modules, Sweden) observation class ROV carrying an extensive
130 sensor suite described in Katlein et al. (Katlein et al., 2017). After each ROVnet deployment,



131 the nets were rinsed with ambient sea-water to concentrate the sample in the cod end of the
132 net. The ROVnet sampled horizontal profiles in the water directly below the sea ice. Standard
133 ROVnet profiles were conducted at the ice-water interface, at 5 m and at 10 m depth. The
134 distance covered by each profile ranged between 300 and 600 m. At station 32, the 10 m
135 profile was aborted due to technical failure, and at station 80 no 5 m profile was sampled due
136 to time constraints, and the subsurface sample was discarded due to handling failure (Table
137 1).

138 The concentrated particulate material collected in the cod-end bottle of the gypsum sampling
139 net was mixed with a sample equivalent volume of 98% ethanol, and stored at 4 °C until
140 further analyses (Wollenburg et al., 2018a).

141 At ROVnet sampling stations, ice thickness was estimated through thickness drill holes with a
142 tape measure. To characterize the properties of the ice floes sampled on the floe-wide scale,
143 ice thickness surveys were conducted at each sampling station with a GEM2 (Geophex)
144 electromagnetic induction ice-thickness sensor (Katlein et al., 2018).

145 **2.2 Initial analyses of ROVnet samples**

146 In the home laboratory the samples were rinsed onto a 32 μm mesh using fresh water. The
147 samples were then oven-dried at 50°C for 20 hours. The remaining crystals were transferred
148 into pre-weighed micropaleontological slides, and their weight was determined with a high-
149 precision Sartorius SE2 ultra-microbalance. Under a Zeiss Axio Zoom V16 microscope,
150 pictures were taken with an Axiocam 506 colour camera. We made both overview images of
151 the whole sample and detailed images of individual crystals. From all samples and crystal
152 morphologies, individual crystals were analysed using Raman microscopy, which confirmed
153 that the crystals were gypsum (Wollenburg et al., 2018a). As in some samples both, very large
154 and very small crystals (Figs. S3-S4) were observed, the $>32 \mu\text{m}$ samples were dry-sieved
155 over a 63 μm analysis sieve. The length and width of the cryogenic gypsum crystals in the
156 size fractions $>32 < 63 \mu\text{m}$ and $>63 \mu\text{m}$ was determined with the software application ImageJ
157 on 50 crystals in each sample and size fraction (Schneider et al., 2012) (Tab. 2).

158 **2.3 Initial analyses of ice cores**

159 At all ice stations, sea ice cores for archive purposes and for further measurement of bottom
160 communities were drilled with a 9 cm diameter ice corer (Kovacs Enterprise) and stored at -



161 20°C (Peeken, 2018). One ice-core from station 80 and four bottom slices (10 cm) of ice-
162 cores from station 45 were studied to investigate the gypsum crystal morphologies within sea
163 ice. Each section was transferred into a measuring jug with lukewarm tap water for approx.
164 two seconds, and then the jug was emptied over a 32 μm analysis sieve, and repeatedly
165 refilled. This process was continued until all ice was melted. With the aid of a hand shower
166 and a wash bottle the residue on the sieve was rinsed and transferred into a 30 μm mesh-
167 covered funnel, dried and transferred into a micropaleontological picking tray for inspection
168 and documentation. For storage, the residue was transferred into pre-weighed labelled
169 micropaleontological slides.

170 **2.4 Dissolution experiments**

171 The aim of our dissolution experiments was to investigate the persistence of gypsum crystals
172 against dissolution in the Arctic water column (water mass trials) and under common
173 biological sample treatment (Formaldehyde trial).

174 Dissolution experiments were carried out on individual gypsum crystals collected from
175 ROVnet samples. Hereby, 5 cryogenic gypsum crystals with different crystal morphologies,
176 and from both size fractions were used in each reaction chamber. Before the start and after the
177 termination of each experiment, pictures of the cryogenic gypsum crystals used were taken
178 with an Axiocam 506 colour camera under a Zeiss Axio Zoom V16 microscope. The weight
179 of the crystals before and after each treatment was determined with a high-precision Sartorius
180 SE2 ultra-microbalance after they had been transferred into a pre-weighted silver boat. The
181 experimental running time of each experiment was 24 hours.

182 **2.4.1 Water mass trials**

183 The experiments to simulate dissolution within the different water masses and hydrostatic
184 pressure regimes of the Arctic Ocean were carried out with high-pressure chambers installed
185 in a cooling table (Wollenburg et al., 2018b). With a high-pressure pump (ProStar218 Agilent
186 Technologies), peak tubing, and multiple titanium valves a continuous isobaric and isocratic
187 one-way seawater flow of 0.3 ml/min was directed through a set of four serially arranged
188 high-pressure chambers each with an internal volume of 0.258 ml (Wollenburg et al., 2018b).
189 This setup allowed for dissolution experiments at defined pressures and temperatures
190 (Wollenburg et al., 2018b). For the experiments, we used sterile-filtered (0.2 μm mesh) North
191 Sea water that was adjusted to a salinity of 34.98 by addition of 1 g Instant Ocean® sea salt



192 per L and psu-offset. The natural pH of 8.1 after equilibration to the refrigerator's atmosphere
193 (at 2.5 °C and at atmospheric pressure), lowers to pH 8.05 at 2.5 °C at 150 bar (Culberson and
194 Pytkowicz, 1968). Five experiments, with 4 high-pressure chambers were carried out. The
195 Polar Surface (PSW) water corresponding experimental trial was running at -0.5 °C and 3 bar,
196 the experimental Atlantic Water (AW) trial at +2.5 °C and 65 bar, and three experimental
197 Deep Water trials were conducted at -1 °C and 100, 120 and 150 bar, respectively.

198 **2.4.2 Formaldehyde trial**

199 To study the effect of Formaldehyde treatment on cryogenic gypsum, the crystals were
200 subjected to a Formaldehyde solution of 4% in seawater, which is commonly used to preserve
201 biological samples. The stock solution consisted of 500 ml Formaldehyde concentration of
202 40%, 500 ml aqua dest. and 100 g hexamethylenetetramine, adjusted to a pH of 7.3-7.9.
203 Aliquots of the 20% stock solution were added to the four-fold volume of artificial Arctic
204 Ocean sea water to obtain a final concentration of 4%.

205 The Gypsum crystals were transferred into Falcon Tubes, and the 4% Formaldehyde solution
206 was added. The Falcon tubes were then either stored at 3 °C, or at room temperature. After
207 the experiments, the gypsum crystal-Formaldehyde suspension was washed with deionized
208 water over a 10 µm mesh using a wash bottle, and dried on gauze. As in all formaldehyde
209 trials all gypsum dissolved, no post-experimental weight was determined.

210

211 **2.5 Size-specific settling velocities of gypsum**

212

213 The size-specific sinking velocity of cryogenic gypsum was measured in a settling cylinder
214 (Ploug et al., 2008). The cylinder (30 cm high and 5 cm in diameter) was filled with filtered
215 seawater (salinity 32) and surrounded by a water jacket for thermal stabilization at 2 °C. The
216 settling cylinder was closed at both ends, only allowing insertion of a wide-bore pipette at the
217 top. Immediately before measurement, the gypsum was submerged into seawater with a
218 salinity of 32 and a temperature of 2 °C, and then transferred to the settling cylinder with a
219 wide-bore pipette. The gypsum crystals were allowed to sink out of the wide-bore pipette,
220 which was centered in the cylinder. The descent of the pellets was recorded by a Basler 4
221 MPixel Ethernet camera equipped with a 25 mm fixed focal lens (Edmund Optics). The
222 settling column was illuminated from the sides by a custom-made LED light source. The
223 camera recorded 7 images per second as the gypsum crystals sank through the settling
224 column. The setup was calibrated by recording a length scale before sinking velocity
225 measurements. The size and settling of the individual gypsum crystals was determined with



226 the image analysis software ImageJ. This was done by using the projected area of the crystals
227 to calculate the equivalent spherical diameter and the distance traveled between the
228 subsequent images to determine the sinking velocity of the individual crystals (Iversen et al.,
229 2010)

230 We calculated the excess density ($\Delta\rho$) ($\Delta\rho = \text{gypsum density} - \text{water density}$) of the crystal
231 from the Stokes drag equation:

232

$$233 \quad \Delta\rho = \frac{C_D \rho_w SV^2}{\frac{4}{3}gESD} \quad (1)$$

234

235 where C_D is the dimensionless drag force (equation 2), ρ_w is the density of seawater (1.0256 g
236 cm³, for a salinity of 32 at 2 °C), SV is the measured sinking velocity in cm s⁻¹, g is the
237 gravitational acceleration of 981 cm s⁻², and ESD is the equivalent spherical diameter in cm.

238 We calculated C_D using the drag equation for low Reynolds numbers (White, 1974):

239

$$240 \quad C_D = \left(\frac{24}{Re}\right) + \left(\frac{6}{1+Re^{0.5}}\right) + 0.4 \quad (2)$$

241

242 where the Reynolds number (Re) was defined as

243

$$244 \quad Re = SV ESD \frac{\rho_w}{\eta} \quad (3)$$

245

246 where η is the dynamic viscosity (1.7545 × 10⁻³ g cm⁻¹ s⁻¹ for a salinity of 32 at 2 °C). Equation
247 2 is valid up to a Reynolds number of 2 × 10⁵ (Vogel and Beety, 1994). The gypsum crystals
248 had Reynolds numbers ranging from 0.77 to 128.

249

250 **2.6 Backtracking the sampled ice flows under which cryogenic gypsum was sampled**

251

252 To determine sea ice drift trajectories of sampled sea ice we used a Lagrangian approach
253 (IceTrack) that traces sea ice backward or forward in time using a combination of satellite-
254 derived low resolution drift products. So far, IceTrack has been used in a number of
255 publications to examine sea ice sources, pathways, thickness changes and atmospheric
256 processes acting on the ice cover (Damm et al., 2018; Peeken, 2018 #13678; Krumpfen et al.,
257 2016; Peeken et al., 2018). A detailed description is provided in Krumpfen et al. (Krumpfen et
258 al., 2019).



259 Sea ice motion information was provided by different institutions, obtained from different
260 sensors, and for different time intervals. In this study we applied a combination of three
261 different products: (i) motion estimates based on a combination of scatterometer and
262 radiometer data provided by the Center for Satellite Exploitation and Research (CERSAT
263 (Girard-Ardhuin and Ezraty, 2012), (ii) the OSI-405-c motion product from the Ocean and
264 Sea Ice Satellite Application Facility (OSISAF (Lavergne, 2016), and (iii) Polar Pathfinder
265 Daily Motion Vectors from the National Snow and Ice Data Center (NSIDC (Tschudi et al.,
266 2016).

267 The tracking approach works as follows: An ice parcel is traced backward or forward in time
268 on a daily basis. Tracking is stopped if a) ice hits the coastline or fast ice edge, or b) ice
269 concentration at a specific location drops below 50% and we assume the ice to be formed.
270 The applied sea ice concentration product was provided by CERSAT and was based on
271 85 GHz SSM/I brightness temperatures, using the ARTIST Sea Ice (ASI) algorithm.

272

273 **3 Results**

274 **3.1 Presence and distribution of cryogenic gypsum under the investigated ice-floes**

275 Based on backtracking (Krumpfen, 2018) and sea ice observations, the sampled ice-floes had
276 an age of 1 to 3 years (Fig. 1B) and were originating from the Siberian Sea (station 32/80), the
277 Laptev Sea (station 45), and were more locally grown in the Nansen Basin (station 66).

278 Whereas the mean sea ice thickness at the ROV survey stations ranged between 94 and 156
279 cm, the mean sea ice thickness of the investigated ice-floes estimated by an ice-thickness
280 sensor surveys (Katlein et al., 2018) was 1.90 m for station 32, 1.00 m for station 45, and 1.80
281 m for stations 66 and 80 (Fig. 1A, Table 1). Despite the different origins and thicknesses of
282 sea ice, cryogenic gypsum crystals were found at all stations and in all depth layers sampled
283 with the ROVnet (Figs. 1A, B, Tab. 1). At all stations and sampling depths the samples were
284 dominated by cryogenic gypsum, with a proportional dry weight of >96.5% in the 5 m-sample
285 at station 32, and with >99% in all other samples (Figs. 2, Figs. S1-S4). Other lithogenic
286 particles, as often found in sea ice (Nürnberg et al., 1994), were essentially absent.

287 **3.2 The morphology of cryogenic gypsum**



288 The samples collected at station 32 were dominated by rounded, matte, solid cryogenic
289 gypsum crystals with a mean length-width ratio of 1.40-1.76 (Tab. 2, S1). The proportional
290 mass contribution of the smaller-sized crystals of the $>30<63 \mu\text{m}$ size fraction increased with
291 depth and outweighed the contribution of the $>63 \mu\text{m}$ size fraction with 56.30%, and 66.28%
292 for the 0 and 5 m water depth sample, respectively (Fig. 3). At 0 m, the mean length of the
293 crystals was $68.46 \mu\text{m}$ in the $>63 \mu\text{m}$ size fraction and $44.27 \mu\text{m}$ in the $>30<63 \mu\text{m}$ fraction.
294 At 5 m depth, crystal dimensions were similar, ranging at mean crystal lengths of $63.28 \mu\text{m}$ in
295 the $>63 \mu\text{m}$, and $35.90 \mu\text{m}$ in the $>30<63 \mu\text{m}$ size fraction, respectively.

296 At station 45, the crystals were mostly solid and for most part hyaline, rather than matte
297 crystals as at station 32 (Figs. 2C-D, 6, S2). With decreasing weight proportion, the $>63 \mu\text{m}$
298 size clearly dominated the 0, 5, and 10 m samples with 79.90, 73.39, and 66.14%,
299 respectively. In the 0 m layer samples, mean crystal lengths were $114.18 \mu\text{m}$ in the $>63 \mu\text{m}$
300 size fraction and $58.74 \mu\text{m}$ in the $>30<63 \mu\text{m}$ size fraction (Tab. 2). At 5 m depth, we
301 observed mean crystal lengths of $111 \mu\text{m}$ in the $>63 \mu\text{m}$ size fractions, and $56.73 \mu\text{m}$ in the
302 $>30<63 \mu\text{m}$ fraction. The mean crystal lengths in the 10 m sample was 92.83 and $50.32 \mu\text{m}$
303 for the >63 and $>30<63 \mu\text{m}$ size fraction, respectively. At station 45 the crystal length-width
304 ratio varied between 1.37 and 1.98, measured in the $>30<63 \mu\text{m}$ size fraction of the surface
305 sample, and the $>63 \mu\text{m}$ size fraction of the 10 m sample. The cryogenic gypsum crystals
306 retrieved from the melted ice core drilled at this station were solid and hyaline. In size and
307 shape they resembled the crystals of the 10 m layer at this station, with a mean crystal length
308 of $114.2 \mu\text{m}$, mean width of $57.2 \mu\text{m}$, and a length-width ratio of 2 (Fig. 4).

309 At station 66, the crystals from 0 m water depth were dominated by large, pencil-like, hyaline
310 and solid crystals with a mean crystal length of $1,355 \mu\text{m}$ and mean width of $415 \mu\text{m}$ in the
311 dominating $>63 \mu\text{m}$ fraction (99.25% mass) (Fig. 2B, S3, Tab. 2). These crystals with an
312 average length-width ratio of 3.27 were found as isolated crystals, but very often also as inter-
313 grown crystal rosettes with two to more than 10 individual crystals involved (Fig. S3; Tab. 2).
314 The $>30<63 \mu\text{m}$ size fraction (0.75% mass) was dominated by matte, whitish, rounded
315 gypsum particles and tiny gypsum needles with a mean crystal length of $56.67 \mu\text{m}$ (Fig. S3,
316 Tab. 2). As at the other stations the weight proportion of the $>63 \mu\text{m}$ size fraction
317 significantly decreased from 99.25 in the 0 m, to 75.23 at 5 m, and 61.18% in the 10 m
318 sample (Fig. 2). The size of cryogenic gypsum crystals collected from the 5 and 10 m layers
319 was significantly smaller and predominantly composed of isolated small hyaline and euhedral
320 gypsum needles. The length-width ratio ranged between 5.60 (5 m) and 4.37 (10 m) (Figs.



321 2A, S3, Tab. 2). In the 5 m layer sample, the mean crystal length was 411.42 μm in the >63
322 μm size fraction, and 62.03 μm in the $>30<63$ μm size fraction. The 10 m samples showed a
323 mean crystal length of 101.40 μm in the >63 , and 30.71 μm in the $>30<63$ μm size fraction
324 (Tab. 2).

325 In the 10 m layer sample of station 80, large tabular gypsum crystals measuring up to 1 cm in
326 length (mean length: 3,078 μm , mean width: 1,830 μm) dominated the >63 μm size fraction.
327 Their average length-width ratio was 1.7. This size fraction contributed 89.1% of the gypsum
328 mass (Figs. 5, S4, Tab. 2). The $>30<63$ μm size fraction was composed of fragments of these
329 large crystals and few small gypsum needles. These often intergrown columnar crystals
330 looked bladed, for most part also dented and with numerous cracks. Their mean length was
331 71.8 μm . The ice core retrieved from this station was very porous and broke into pieces of 9
332 to 11 cm. Cryogenic gypsum was retrieved from all these ice core sections and revealed a
333 dominance of extraordinary large crystals (Figs. 5, S4), resembling the ROVnet samples from
334 this station. The largest cryogenic gypsum crystals $>6,000$ μm (mean crystal length: 2,821
335 μm , mean width: 1,689 μm) were retrieved from the top-most 8 cm ice core section, whereas,
336 the maximum crystal size gradually decreased downcore (Fig. S4). The crystals themselves
337 lacked sharp corners, and the large crystals had cavities inside, indicating an advanced stage
338 of dissolution (Figs. 5C-D; S4).

339

340 3.3 Dissolution experiments

341 3.3.1 Experiments to simulate cryogenic gypsum dissolution within the Arctic water 342 column

343 Our study area was characterized by the presence of three main water masses (Nikolopoulos
344 et al., 2018; Rudels, 2015): 1) The Polar Surface Water (PSW) including the halocline, with a
345 variable mean salinity of 32 and a temperature range of -1.8 to 0.0 °C, extended from the
346 surface to maximum 100 m water depth (Nikolopoulos et al., 2018). 2) The Atlantic Water
347 (AW) with a mean salinity of 34.4 to 34.7 and variable temperature of 0.0 to 4.7 °C in the
348 study area extended from below the PSW to 600-800 m water depth (Nikolopoulos et al.,
349 2018). 3) The Eurasian Arctic Deep Water (EADW) fills the deep Eurasian Basin below the
350 AW with a temperature range of <0 to -0.94 °C and a salinity of about 34.9 (Nikolopoulos et
351 al., 2018).



352 The dissolution experiments carried out to simulate dissolution in the PSW were set to 3 bar,
353 $-0.5\text{ }^{\circ}\text{C}$. Over the 24 hours lasting PSW-simulating dissolution experiment, about 6% of the
354 gypsum dissolved (Figs. 6, S5A, Tab. 3). In the AW experiment, the combination of positive
355 temperatures ($2.5\text{ }^{\circ}\text{C}$) and a pressure of 65 bar impacted the dissolution on the cryogenic
356 gypsum crystals more than in any other seawater trial. More than 80% of the cryogenic
357 gypsum crystals dissolved during the 24-hours experiment (Figs. 6, S5B, Tab. 3). Moreover,
358 as dissolution mainly affects the crystal's surface, smaller gypsums crystals and those with
359 increased surface roughness were preferentially impacted by dissolution, whereas larger and
360 solid crystals with smooth surface showed the lowest dissolution (Fig. S5B). The EADW-
361 simulating dissolution experiments set to a temperature of $-0.5\text{ }^{\circ}\text{C}$ showed a progressive
362 cryogenic gypsum dissolution of 26, 58, and 62% with increasing pressure for the 100, 120
363 and 150 bar experiments, respectively (Figs. 6, S6, Tab. 3).

364 **3.3.2 Experiments to simulate cryogenic gypsum dissolution within Formaldehyde-** 365 **treated biological samples**

366 In the Formaldehyde experiments we exposed our set of cryogenic gypsum crystals to a
367 Formaldehyde solution of 4%, which is commonly used to store pelagic samples from the
368 Polar Oceans (Edler, 1979). Irrespective of the temperature at which the sample was stored,
369 all gypsum dissolved within 24 hours.

370 **3.4 Sinking velocities of gypsum crystals**

371

372 The sinking velocity (SV) of the gypsum crystals increased with crystal size (Fig. 7A). Small
373 crystals with an equivalent spherical diameter (ESD) of $200\text{ }\mu\text{m}$ sank with 300 m d^{-1} while
374 large gypsum crystals with $ESDs$ of $2,000$ to $2,500\text{ }\mu\text{m}$ sank with velocities of $5,000$ to $7,000$
375 m d^{-1} . The size to settling relationship was best described by a power function ($SV = 4239.9$
376 $ESD^{0.89}$, $R^2 = 0.84$). As the power function suggests, the settling velocity levelled off for the
377 largest gypsum crystals (Fig. 7A). The observed excess density of all crystals was smaller
378 than is expected from the density of gypsum (2310 kg/m^3). For the visually non porous
379 smaller crystals drag, the deviation of gypsum crystals from round particles, and dissolution
380 may be the main reason for the calculated lower density.

381 However, plotting the excess density as a function of size (Fig. 7B) also showed that the
382 excess density of the gypsum decreased with increasing crystal size. The microscopic images
383 show that large crystals were more porous and had more complex shapes (Fig. S8 A-C)



384 compared to the small crystals that were more spherical and less porous (Figs. 2, 4-5, S8 D).
385 Hence, the flat settling to size relationship for large gypsum crystals (Fig. 7A), was essentially
386 due to a combination of increased porosity causing decreasing excess density and increased
387 drag due to the complex shapes of the large crystals.

388

389 **4 Discussion**

390

391 **4.1 Distribution and morphology of cryogenic gypsum crystals**

392

393 This study shows for the first time the wide-spread presence of cryogenic gypsum under melting
394 Arctic sea ice of different origin. At all stations cryogenic gypsum dominated the sample
395 fraction of particles $>30\ \mu\text{m}$ in Eurasian Basin surface waters, indicating a continuous cryogenic
396 gypsum flux from warming sea ice over a period of six weeks.

397 When designing the ROVnet for cryogenic gypsum sampling, we opted for the coarser $>30\ \mu\text{m}$
398 mesh to prohibit an overflow of the sampling container when running into a phytoplankton
399 bloom. However, as Geilfus et al. (Geilfus et al., 2013) had observed gypsum crystals as small
400 as $10\ \mu\text{m}$, we probably lost an unknown proportion of smaller gypsum crystals by the chosen
401 sampling strategy. The gypsum crystals described from sea ice so far retrieved from only 3-
402 days-old experimental and 30 cm thick natural sea ice off Greenland were small (crystal length
403 max. $100\ \mu\text{m}$), planar euhedral gypsum crystals often intergrown or as rosettes (Geilfus et al.,
404 2013). Similar, but larger (crystal length up to 1 mm), gypsum crystals were observed within
405 *Phaeocystis* aggregates collected in the region of the present study (Wollenburg et al., 2018a).
406 However, here we show that gypsum crystals exhibit a strong variability in size and
407 morphology. Particularly large crystals were characterised by more complex shapes (Fig. 2, 5,
408 S3-4) and increased porosity (Figs. S6A-C), compared to the small planar euhedral (Fig. 2A)
409 and more spherical crystals (Fig. S6D). Euhedral crystal needles larger but otherwise similar to
410 those described by Geilfus et al. (Geilfus et al., 2013) and Wollenburg et al. (Wollenburg et al.,
411 2018a) dominated the $>63\ \mu\text{m}$ fraction collected at 5 and 10 m depths at station 66, and smaller
412 crystals contributed especially to the $>30<63\ \mu\text{m}$ size fraction of the station's subsurface
413 samples.

414 As cryogenic gypsum forms in sea ice brine pockets or channels, the size and morphology
415 especially of large crystals is likely determined by sea ice texture and porosity during gypsum



416 precipitation. Pursuing this hypothesis, the large and intergrown crystals collected from the
417 0 m layer at station 66, and the 10 m layer and ice-core at station 80, formed in highly
418 branched granular sea ice (Lieb-Lappen et al., 2017; Weissenberger et al., 1992). In contrast,
419 the small cryogenic gypsum needles reported by Geilfus et al. (Geilfus et al., 2013) and
420 Wollenburg et al. (Wollenburg et al., 2018a), may have preferentially formed in columnar sea
421 ice. Even sampling the same ice-floe (station 32 and 80), the appearance of the crystals
422 changed. Possibly, a widening of the brine channels during the elapsed time (6 weeks)
423 allowed a release of larger crystals at station 80 when compared to station 32. However,
424 crystal growth during this elapsed period or lateral advection of large crystals cannot be
425 excluded. Thus, detailed texture analyses on sea ice cores prior to sampling are needed to
426 validate or reject hypotheses on a link between sea ice porosity and cryogenic gypsum crystal
427 size and morphology and should be considered in future studies.

428 The sea ice microstructure dictating the formation of gypsum crystals in the brine matrix
429 likely varied among ice-floes due to different ages, origins and drift trajectories (Fig. 1B). For
430 example, station 66 was the only station where the sea ice likely formed over the central
431 Nansen Basin only months before our study (Fig. 1B). The surface sample of station 66 had
432 large intergrown hyaline star-shaped gypsum crystals that were observed at no other station.
433 They also showed a considerably higher length-width ratio than crystals from second-year ice
434 of stations 32/80 and 45 (Fig. 1B; Fig. 2). Accordingly, a close relationship between local sea
435 ice properties and gypsum crystal morphology in the underlying water was evident from the
436 comparison of gypsum crystals collected with the ROVnet with those retrieved from ice cores
437 collected at two stations. The ice-core samples revealed cryogenic gypsum crystals that
438 basically resembled the crystal morphologies collected from the water column at these
439 stations, indicating that the gypsum morphologies observed in the water column likely reflect
440 the gypsum precipitation conditions and brine-channel structure of local ice-floes. The current
441 understanding of mineral precipitation in supersaturated brines relies on ice-core analyses, sea
442 ice brine- and experimental studies, and on mathematical modelling of the temperature
443 window in which each mineral is likely to form (Butler et al., 2017; Marion et al., 2010).
444 There are still many uncertainties regarding the precipitation and dissolution of gypsum
445 within natural sea ice and during ice-core storage. Although the FREZCHEM model and
446 Gitterman Pathway predict gypsum precipitation under defined conditions, only Geilfus et al.
447 (Geilfus et al., 2013) and Butler et al. (Butler et al., 2017) succeeded in retrieving gypsum
448 under such conditions, whereas others failed (Butler and Kennedy, 2015). According to the
449 FREZCHEM model, cryogenic gypsum precipitates at temperatures of -6.2 to -8.5 °C and at



450 temperatures < -18 °C (Geilfus et al., 2013; Wollenburg et al., 2018a). Accordingly, a storage
451 temperature of -20 °C would allow the post-coring precipitation of gypsum from contained
452 brines. However, in field and experimental studies cryogenic gypsum was so far only
453 observed to precipitate in the -6.2 to -8.5 °C temperature window, even when treatments were
454 conducted below -20 °C (Butler et al., 2017; Geilfus et al., 2013). Furthermore, the observed
455 signs of dissolution on the large cryogenic gypsum crystals from the ice-core when compared
456 to the sharp-edged crystals retrieved from the water column at station 80 indicate that
457 significant new precipitation of gypsum during storage did not occur, rather the opposite.

458 Apart from the growing conditions of gypsum crystals within sea ice, the size spectrum of
459 crystals retrieved from different depths in the water column likely was essentially altered by
460 the size-dependent sinking velocity of the crystals. Because the sinking velocity of large
461 cryogenic gypsum crystals is high the chance to catch large crystals with horizontal transects
462 directly under the ice should be lower compared to small crystals (Fig. 7A). Accordingly,
463 significant amounts of large cryogenic gypsum crystals were mainly sampled from the 0 m
464 layer where they could be scraped off the underside of the ice (see station 66, Tab. 2). In
465 contrast, smaller cryogenic gypsum crystals sink at lower velocities (Fig. 7A). Hence, the
466 large quantity of small-sized crystals retrieved in the deeper layers of station 66, and all layers
467 of station 32 and 45 likely were influenced by the accumulated gypsum release in this size-
468 fraction, whereas the rarer large crystals indicated the momentary release at these stations.
469 The extremely large crystals sampled at station 80 at 10 m depth probably indicated an on-
470 going flux event during rapid melting. According to our dissolution experiments, gypsum
471 dissolution within Arctic surface waters should only have a minor impact on the size
472 distribution of cryogenic gypsum crystals within the surface water. Besides vertical flux,
473 advection of gypsum crystals with surface currents may also have influenced the size-
474 distribution of gypsum crystals sampled in the water column.

475

476 **4.2 Reasons why cryogenic gypsum was rarely observed in past studies**

477

478 The small temperature range of the -6.2 to -8.5 °C window, which is also the only gypsum
479 precipitation temperature spectrum applicable in the Arctic Ocean, has been considered one
480 reason why gypsum was not detected in other studies (Butler and Kennedy, 2015; Wollenburg
481 et al., 2018a). Furthermore, the kinetics of gypsum precipitation was considered as too slow
482 for detection during experimental studies, and the amount of gypsum hard to verify versus



483 other sea ice precipitates that are quantitatively much more abundant, leading the focus
484 towards other sea ice precipitates (Butler and Kennedy, 2015; Geilfus et al., 2013). Although
485 cryogenic mirabilite and hydrohalite are three and twenty-two times more abundant than
486 gypsum, respectively (Butler and Kennedy, 2015), gypsum is the only sea ice precipitate that
487 survives for one to several days within the Arctic water column. Cryogenic gypsum
488 dissolution increases with increasing hydrostatic pressure and increasing temperatures (Fig.
489 6). However, well preserved cryogenic gypsum crystals were retrieved from algae aggregates
490 collected from 2,146 m water depth, suggesting that either the transport from the surface to
491 this depth was very rapid or that dissolution was decreased and/or prevented once gypsum
492 crystals were included within the matrix of organosulfur compound-rich aggregates
493 (Wollenburg et al., 2018a). Yet, as seawater is usually undersaturated with respect to gypsum
494 (Briskin and Schreiber, 1978a; Briskin and Schreiber, 1978b) and is shown by our dissolution
495 experiments, disaggregation of organic aggregates would expose the gypsum to the seawater
496 and dissolve any crystals making it to the deep ocean or seafloor likely within a few days. The
497 same dissolution would occur within the sampling cups of sediment traps, explaining why
498 gypsum has not been observed in those type of samples.

499 Our dissolution experiments showed that cryogenic gypsum can persist long enough in the
500 cold polar surface water to be collected in measurable concentrations. The missing evidence
501 of gypsum from past studies was likely due to the quick dissolution of gypsum crystals at
502 higher temperatures and pressure dependence of dissolution kinetics, impeding the discovery
503 of gypsum in sediment trap samples and on the sea-floor. In addition, Formaldehyde
504 preservation leads to the immediate dissolution of gypsum, too, destroying any evidence of
505 cryogenic gypsum in all kinds of biological samples including water column and net samples.

506

507 **4.3 Potential of cryogenic gypsum as a ballast of algae blooms**

508

509 We found less than 6% dissolution of individual crystals in Polar Surface Water (PSW) per
510 day. Thus, at depths immediately below the fluorescence maximum where a significant part
511 of organic aggregates are formed (Iversen et al. 2010), the gypsum scavenging and ballasting
512 of aggregates (Turner, 2015) is little affected by gypsum dissolution (Olli et al., 2007) (Fig. 6,
513 Tab. 3). Incorporation of dense minerals into settling organic aggregates will increase their
514 density and, therefore, the size-specific sinking velocities of the aggregates (Iversen and
515 Ploug, 2010; Iversen and Robert, 2015; van der Jagt et al., 2018). The high sinking velocity of
516 large gypsum crystals >1 mm (5,000-7,000 m d⁻¹ (Fig. 7A)) could create strong hydrodynamic



517 shear that might cause disaggregation of fragile algae aggregates (Olli et al., 2007). This
518 supports previous suggestions of gypsum as an important ballast mineral of organic
519 aggregates, such as *Phaeocystis* (Wollenburg et al., 2018a) by rather small crystals.
520 As chlorophyll concentrations in the surface water were mostly low ($< 1 \text{ mg m}^{-3}$, H.F.
521 unpublished data), a massive gypsum-mediated export of phytoplankton was unlikely during
522 expedition PS106. However, especially at the ice floe of station 32/80, we observed a high
523 coverage of the ice underside by the filamentous algae *Melosira arctica*, and gypsum crystals
524 were found in *M. arctica* filaments collected nearby (Figs. 2D, 8). This indicates a potential
525 for rapid *M. arctica* downfall mediated by cryogenic gypsum, as soon as the algal filaments
526 were released from the melting sea ice. Hence, ballasting by cryogenic gypsum may also have
527 contributed to the mass export of *Melosira arctica* aggregates observed in 2012 (Boetius et al.
528 2013).

529

530

531 **5 Conclusions**

532 This study shows for the first time that gypsum released to the water at the onset of melt
533 season in the Arctic Ocean causes a constant flux of gypsum over wide spread areas and over
534 a long period of time ($> \text{six weeks}$). The morphological diversity of gypsum crystals retrieved
535 from Arctic surface waters and ice-cores indicated a complex variety of precipitation and
536 release processes as well as modifications during sea ice formation, the melt phase, and in the
537 water column. In the fresh and cold Polar surface water, gypsum crystals persist long enough
538 to act as an effective ballast on organic matter, such as phytoplankton filaments and marine
539 snow.

540

541 **References:**

542 Arrigo, K. R., Perovich, D. K., Pickart, R. S., Brown, Z. W., van Dijken, G. L., Lowry, K. E., Mills,
543 M. M., Palmer, M. A., Balch, W. M., Bahr, F., Bates, N. R., Benitez-Nelson, C., Bowler, B.,
544 Brownlee, E., Ehn, J. K., Frey, K. E., Garley, R., Laney, S. R., Lubelczyk, L., Mathis, J., Matsuoka,
545 A., Mitchell, B. G., Moore, G. W. K., Ortega-Retuerta, E., Pal, S., Polashenski, C. M., Reynolds,
546 R. A., Schieber, B., Sosik, H. M., Stephens, M., and Swift, J. H.: Massive Phytoplankton
547 Blooms Under Arctic Sea Ice, *Science*, 336, 1408, 2012.
548
549 Arrigo, K. R., Perovich, D. K., Pickart, R. S., Brown, Z. W., van Dijken, G. L., Lowry, K. E., Mills,
550 M. M., Palmer, M. A., Balch, W. M., Bates, N. R., Benitez-Nelson, C. R., Brownlee, E., Frey, K.
551 E., Laney, S. R., Mathis, J., Matsuoka, A., Greg Mitchell, B., Moore, G. W. K., Reynolds, R. A.,
552 Sosik, H. M., and Swift, J. H.: Phytoplankton blooms beneath the sea ice in the Chukchi sea,
553 *Deep Sea Research Part II: Topical Studies in Oceanography*, 105, 1-16, 2014.



- 554 Assmy, P., Fernández-Méndez, M., Duarte, P., Meyer, A., Randelhoff, A., Mundy, C. J., Olsen,
555 L. M., Kauko, H. M., Bailey, A., Chierici, M., Cohen, L., Doulgeris, A. P., Ehn, J. K., Fransson, A.,
556 Gerland, S., Hop, H., Hudson, S. R., Hughes, N., Itkin, P., Johnsen, G., King, J. A., Koch, B. P.,
557 Koenig, Z., Kwasniewski, S., Laney, S. R., Nicolaus, M., Pavlov, A. K., Polashenski, C. M.,
558 Provost, C., Rösel, A., Sandbu, M., Spreen, G., Smedsrud, L. H., Sundfjord, A., Taskjelle, T.,
559 Tatarek, A., Wiktor, J., Wagner, P. M., Wold, A., Steen, H., and Granskog, M. A.: Leads in
560 Arctic pack ice enable early phytoplankton blooms below snow-covered sea ice, *Scientific*
561 *Reports*, 7, 40850, 2017.
- 562
- 563 Briskin, M. and Schreiber, B. C.: Authigenic gypsum in marine sediments, *Marine Geology*,
564 28, 37-49, 1978.
- 565
- 566 Butler, B.: Mineral dynamics in sea ice brines, PhD, Bangor, 184 pp., 2016.
- 567
- 568 Butler, B. M. and Kennedy, H.: An investigation of mineral dynamics in frozen seawater
569 brines by direct measurement with synchrotron X-ray powder diffraction, *Journal of*
570 *Geophysical Research: Oceans*, 120, 5686-5697, 2015.
- 571
- 572 Butler, B. M., Papadimitriou, S., Day, S. J., and Kennedy, H.: Gypsum and hydrohalite
573 dynamics in sea ice brines, *Geochimica et Cosmochimica Acta*, 213, 17-34, 2017.
- 574
- 575 Culberson, C. and Pytkowicz, R. M.: Effect of pressure on carbonic acid, boric acid, and the
576 pH in seawater, *Limnology and Oceanography*, 13, 403-417, 1968.
- 577
- 578 Damm, E., Bauch, D., Krumpen, T., Rabe, B., Korhonen, M., Vinogradova, E., and Uhlig, C.:
579 The Transpolar Drift conveys methane from the Siberian Shelf to the central Arctic Ocean,
580 *Scientific Reports*, 8, 4515, 2018.
- 581
- 582 Docquier, D., Massonnet, F., Barthélemy, A., Tandon, N. F., Lecomte, O., and Fichet, T.:
583 Relationships between Arctic sea ice drift and strength modelled by NEMO-LIM3.6, *The*
584 *Cryosphere*, 11, 2829-2846, 2017.
- 585
- 586 Edler, L.: Recommendations on Methods for Marine Biological Studies in the Baltic Sea:
587 Phytoplankton and chlorophyll, Department of Marine Botany, University of Lund, 1979.
- 588
- 589 Flores, H. E., J.; Lange, B.; Sulanke, E.; Niehoff, B.; Hildebrandt, N.; Doble, M.; Schaafsma, F.;
590 Meijboom, A.; Fey, B.; Kühn, S.; Bravo-Rebolledo; E.; Dorssen, M. van; Gradinger, R.;
591 Hasset, B.; Kunisch, E.; Kohlbach, D.; Graeve, M.; Franeker, J. A. van; Gradinger, Bluhm, B.:
592 Under-ice fauna, zooplankton and endotherms. In: *The Expeditions PS106/1 and 2 of the*
593 *Research Vessel Polarstern to the Arctic Ocean in 2017*, Macke, A. F., H. (Ed.), Reports on
594 polar and marine research, 2018.
- 595
- 596 Geilfus, N. X., Galley, R. J., Cooper, M., Halden, N., Hare, A., Wang, F., Sjøgaard, D. H., and
597 Rysgaard, S.: Gypsum crystals observed in experimental and natural sea ice, *Geophysical*
598 *Research Letters*, 40, 6362-6367, 2013.
- 599



- 600 Girard-Arduin, F. and Ezraty, R.: Enhanced Arctic Sea Ice Drift Estimation Merging
601 Radiometer and Scatterometer Data, *IEEE Transactions on Geoscience and Remote Sensing*,
602 50, 2639-2648, 2012.
- 603
604 Golden, K. M., Ackley, S. F., and Lytle, V. I.: The Percolation Phase Transition in Sea Ice,
605 *Science*, 282, 2238, 1998.
- 606
607 Iversen, M., Nowald, N., Ploug, H., A. Jackson, G., and Fischer, G.: High resolution profiles of
608 vertical particulate organic matter export off Cape Blanc, Mauritania: Degradation processes
609 and ballasting effects, *Deep Sea Research Part I Oceanographic Research Papers*, 57, 771-
610 784, 2010.
- 611
612 Iversen, M. H. and Ploug, H.: Ballast minerals and the sinking carbon flux in the ocean:
613 carbon-specific respiration rates and sinking velocity of marine snow aggregates,
614 *Biogeosciences*, 7, 2613-2624, 2010.
- 615
616 Iversen, M. H. and Robert, M. L.: Ballasting effects of smectite on aggregate formation and
617 export from a natural plankton community, *Marine Chemistry*, 175, 18-27, 2015.
- 618
619 Katlein, C., Arndt, S., Nicolaus, M., Perovich, D. K., Jakuba, M. V., Suman, S., Elliott, S.,
620 Whitcomb, L. L., McFarland, C. J., Gerdes, R., Boetius, A., and German, C. R.: Influence of ice
621 thickness and surface properties on light transmission through Arctic sea ice, *Journal of*
622 *Geophysical Research: Oceans*, 120, 5932-5944, 2015.
- 623
624 Katlein, C., Nicolaus, M., Sommerfeld, A., Copalorado, V., Tiemann, L., Zanatta, M., Schulz,
625 H., and Lange, B.: Sea Ice Physics. In: *The Expeditions PS106/1 and 2 of the research vessel*
626 *Polarstern in the Arctic Ocean in 2017*, Macke, A. F., H. (Ed.), *Berichte zur Polarforschung*
627 *Bremerhaven*, 2018.
- 628
629 Katlein, C., Schiller, M., Belter, H. J., Coppolaro, V., Wenslandt, D., and Nicolaus, M.: A New
630 Remotely Operated Sensor Platform for Interdisciplinary Observations under Sea Ice,
631 *Frontiers in Marine Science*, 4, 281, 2017.
- 632
633 Krumpfen, T.: *AWI ICETrack - Antarctic and Arctic Sea Ice Monitoring and Tracking Tool*
634 *Alfred-Wegener-Institut Helmholtz-Zentrum für Polar- und Meeresforschung, Bremerhaven,*
635 *Germany*, 2018.
- 636
637 Krumpfen, T., Belter, H. J., Boetius, A., Damm, E., Haas, C., Hendricks, S., Nicolaus, M., Nöthig,
638 E.-M., Paul, S., Peeken, I., Ricker, R., and Stein, R.: Arctic warming interrupts the Transpolar
639 Drift and affects long-range transport of sea ice and ice-rafted matter, *Scientific Reports*, 9,
640 5459, 2019.
- 641
642 Krumpfen, T., Gerdes, R., Haas, C., Hendricks, S., Herber, A., Selyuzhenok, V., Smedsrud, L.,
643 and Spreen, G.: Recent summer sea ice thickness surveys in Fram Strait and associated ice
644 volume fluxes, *The Cryosphere*, 10, 523-534, 2016.
- 645
646 Kwok, R.: Arctic sea ice thickness, volume, and multiyear ice coverage: losses and coupled
647 variability (1958–2018), *Environmental Research Letters*, 13, 105005, 2018.



- 648
649 Kwok, R. and Rothrock, D. A.: Decline in Arctic sea ice thickness from submarine and ICESat
650 records: 1958-2008, *Geophys. Res. Lett.*, 36, 2009.
- 651
652 Lavergne, T.: Validation and Monitoring of the OSI SAF Low Resolution Sea Ice Drift Product
653 (v5), 2016.
- 654
655 Lieb-Lappen, R. M., Golden, E. J., and Obbard, R. W.: Metrics for interpreting the
656 microstructure of sea ice using X-ray micro-computed tomography, *Cold Regions Science and
657 Technology*, 138, 24-35, 2017.
- 658
659 Marion, G. M., Mironenko, M. V., and Roberts, M. W.: FREZCHEM: A geochemical model for
660 cold aqueous solutions, *Computers & Geosciences*, 36, 10-15, 2010.
- 661
662 Nicolaus, M., Arndt, S., Katlein, C., Maslanik, J., and Hendricks, S.: Correction to “Changes in
663 Arctic sea ice result in increasing light transmittance and absorption”, *Geophysical Research
664 Letters*, 40, 2699-2700, 2013.
- 665
666 Nicolaus, M., Katlein, C., Maslanik, J., and Hendricks, S.: Changes in Arctic sea ice result in
667 increasing light transmittance and absorption, *Geophysical Research Letters*, 39, 2012.
- 668
669 Nikolopoulos, A., Heuzé, C., Linders, T., Andrée, E., and Sahlin, S.: Physical Oceanography. In:
670 The Expeditions PS106/1 and 2 of the Research Vessel POLARSTERN to the Arctic Ocean in
671 2017, Macke, A. and Flores, H. (Eds.), *Reports on Polar and Marine Research*, Alfred-
672 Wegener Institute Helmholtz Centre for Polar and marine research, Bremerhaven, 2018.
- 673
674 Nürnberg, D., Wollenburg, I., Dethleff, D., Eicken, H., Kassens, H., Letzig, T., Reimnitz, E., and
675 Thiede, J.: Sediments in Arctic sea ice: Implications for entrainment, transport and release,
676 *Marine Geology*, 119, 185-214, 1994.
- 677
678 Olli, K., Wassmann, P., Reigstad, M., Ratkova, T. N., Arashkevich, E., Pasternak, A., Matrai, P.
679 A., Knulst, J., Tranvik, L., Klais, R., and Jacobsen, A.: The fate of production in the central
680 Arctic Ocean - top-down regulation by zooplankton expatriates?, *Progress In Oceanography*,
681 72, 84-113, 2007.
- 682
683 Peeken, I., Primpke, S., Beyer, B., Gütermann, J., Katlein, C., Krumpfen, T., Bergmann, M.,
684 Hehemann, L., and Gerdtts, G.: Arctic sea ice is an important temporal sink and means of
685 transport for microplastic, *Nature Communications*, 9, 1505, 2018.
- 686
687 Peeken, I. C., G.; Flores, H.; Ehrlich, J.; Lange, B.; Schaafsma, F., Gradinger, R.; Hassett, B.;
688 Kunisch, E.; Damm, E.; Verdugo, J.; Kohlbach, D.; Graeve, M.; Bluhm, B.: Sea ice biology and
689 biogeochemistry. In: The Expeditions PS106/1 and 2 of the Research Vessel Polarstern to the
690 Arctic Ocean in 2017, Macke, A. F., H. (Ed.), 719, *Reports of polar and marine research*, 2018.
- 691 Ploug, H., Iversen, M. H., Koski, M., and Buitenhuis, E. T.: Production, oxygen respiration
692 rates, and sinking velocity of copepod fecal pellets: Direct measurements of ballasting by
693 opal and calcite, *Limnology and Oceanography*, 53, 469-476, 2008.



- 694 Rudels, B.: Arctic Ocean circulation, processes and water masses: A description of
695 observations and ideas with focus on the period prior to the International Polar Year 2007–
696 2009, *Progress in Oceanography*, 132, 22-67, 2015.
- 697
698 Schneider, C. A., Rasband, W. S., and Eliceiri, K. W.: NIH Image to ImageJ: 25 years of image
699 analysis, *Nature Methods*, 9, 671, 2012.
- 700
701 Smedsrud, L. H., Halvorsen, M. H., Stroeve, J. C., Zhang, R., and Kloster, K.: Fram Strait sea ice
702 export variability and September Arctic sea ice extent over the last 80 years, *The Cryosphere*,
703 11, 65-79, 2017.
- 704
705 Strunz, H. and Nickel, E. H.: *Strunz Mineralogical Tables. Chemical-structural Mineral
706 Classification System*, Schweizerbart'sche Verlagsbuchhandlung (Nägele u. Obermiller),
707 Stuttgart, 2001.
- 708
709 Tschudi, S., Fowler, C., Maslanik, J., Stewart, J., and Stewart, W.: Polar Pathfinder Daily 25 km
710 EASE-Grid Sea Ice Motion Vectors. In: Technical report, NASA National Snow and Ice Data
711 Center Distributed Active Archive Center, Boulder, Colorado USA 2016.
- 712
713 Turner, J. T.: Zooplankton fecal pellets, marine snow, phytodetritus and the ocean's
714 biological pump, *Progress in Oceanography*, 130, 205-248, 2015.
- 715
716 van der Jagt, H., Friese, C., Stuut, J.-B. W., Fischer, G., and Iversen, M. H.: The ballasting
717 effect of Saharan dust deposition on aggregate dynamics and carbon export: Aggregation,
718 settling, and scavenging potential of marine snow, *Limnology and Oceanography*, 63, 1386-
719 1394, 2018.
- 720
721 Vogel, S. and Beety, S. T.: *Life in Moving Fluids: The Physical Biology of Flow*, Princeton
722 University Press, 1994.
- 723
724 Weissenberger, J., Dieckmann, G., Gradinger, R., and Spindler, M.: Sea ice: A cast technique
725 to examine and analyze brine pockets and channel structure, *Limnology and Oceanography*,
726 37, 179-183, 1992.
- 727
728 White, F. M.: *Viscous fluid flow*, McGraw-Hill, 1974. 614, 1974.
- 729
730 Wollenburg, J. E., Katlein, C., Nehrke, G., Nöthig, E. M., Matthiessen, J., Wolf- Gladrow, D. A.,
731 Nikolopoulos, A., Gázquez-Sanchez, F., Rossmann, L., Assmy, P., Babin, M., Bruyant, F.,
732 Beaulieu, M., Dybwad, C., and Peeken, I.: Ballasting by cryogenic gypsum enhances carbon
733 export in a Phaeocystis under-ice bloom, *Scientific Reports*, 8, 7703, 2018a.
- 734
735 Wollenburg, J. E., Zittier, Z. M. C., and Bijma, J.: Insight into deep-sea life – *Cibicidoides*
736 *pachyderma* substrate and pH-dependent behaviour following disturbance, *Deep Sea
737 Research Part I: Oceanographic Research Papers*, 138, 34-45, 2018b.
- 738
739
740 **Table captions:**



741

Site	Date	Latitude (Deg N)	Longitude (Deg E)	Ocean depth (m)	Sampling depth	Water temp. (°C)	Salinity	Mean ice thickness (m)	Filtered water volume (m ³)
32	2017-06-15	81.73	10.86	1608	under-ice	-1.94	34.27	1.90	2.2
					5 m	n.a.	n.a.	1.90	3.9
45	2017-06-25	78.10	30.47	233	under-ice	-1.52	33.84	1.00	2.3
					5 m	-1.47	34.11	1.00	4.5
					10 m	-1.68	34.29	1.00	2.5
66	2017-07-02	81.66	32.34	1506	under-ice	-1.67	33.18	1.80	3.1
					5 m	-1.71	33.76	1.80	2.7
					10 m	-1.73	33.78	1.80	3.1
80	2017-07-12	81.37	17.13	1010	10 m	-1.37	32.87	1.80	1.7

742

743 Tab. 1: Properties of sea ice stations and characteristics of ROVnet profiles.

744



Cruise, Site, mean water depth of the catch	>63 μm fraction			>30<63 μm fraction			>63 μm fraction weight%	>30<63 μm fraction weight%
	Mean length μm	Mean width μm	length/width ratio	Mean length μm	Mean width μm	length/width ratio		
PS106.1, Stat. 32, 0 m	68.46	44.27	1.55	50.64	35.03	1.45	43.70	56.30
PS106.1, Stat. 32, 5 m	63.28	35.90	1.76	49.91	35.57	1.40	33.72	66.28
PS106.1, Stat. 32, mean (0-5 m)	65.87	40.09	1.64	50.28	35.30	1.42	38.71	61.29
PS106.2, Stat. 45, 0 m	114.18	65.93	1.73	58.74	42.84	1.37	79.90	20.10
PS106.2, Stat. 45, 5 m	110.98	64.84	1.71	56.73	38.89	1.46	73.39	26.61
PS106.2, Stat. 45, 10 m	92.83	46.81	1.98	50.32	29.98	1.68	66.14	33.86
PS106.2, Stat. 45, mean (0-10 m)	85.49	44.45	1.92	77.93	24.28	3.21	73.14	26.86
PS106.2, Stat. 66, 0 m	1355.38	415.10	3.27	56.67	25.63	2.21	99.25	0.75
PS106.2, Stat. 66, 5 m	411.42	73.45	5.60	62.03	12.20	5.08	75.23	24.77
PS106.2, Stat. 66, 10 m	101.40	23.19	4.37	30.71	5.79	5.30	61.18	38.82
PS106.2, Stat. 66, mean (0-10 m)	599.17	164.78	3.64	59.96	12.61	4.76	58.16	41.84
PS106.2, Stat. 80, 10 m	3078.44	1830.00	1.68	71.78	30.76	2.33	89.05	10.95

745

746 Tab. 2: Size measurements and percentage of mass contribution of gypsum crystals from the
 747 >63 μm size fraction and the >30 < 63 μm size fraction

Chamber (no.)/Water mass	Dissolution in weight%				
	PSW	AW	EADW (1)	EADW (2)	EADW (3)
1	11.34	76.22	47.52	57.08	74.92
2	1.33	86.23	26.09	71.03	53.77
3	8.29	82.93	21.05	47.15	57.43
4	2.99	78.57	10.91	58.56	
Mean	5.99	80.77	26.39	58.34	62.04

748

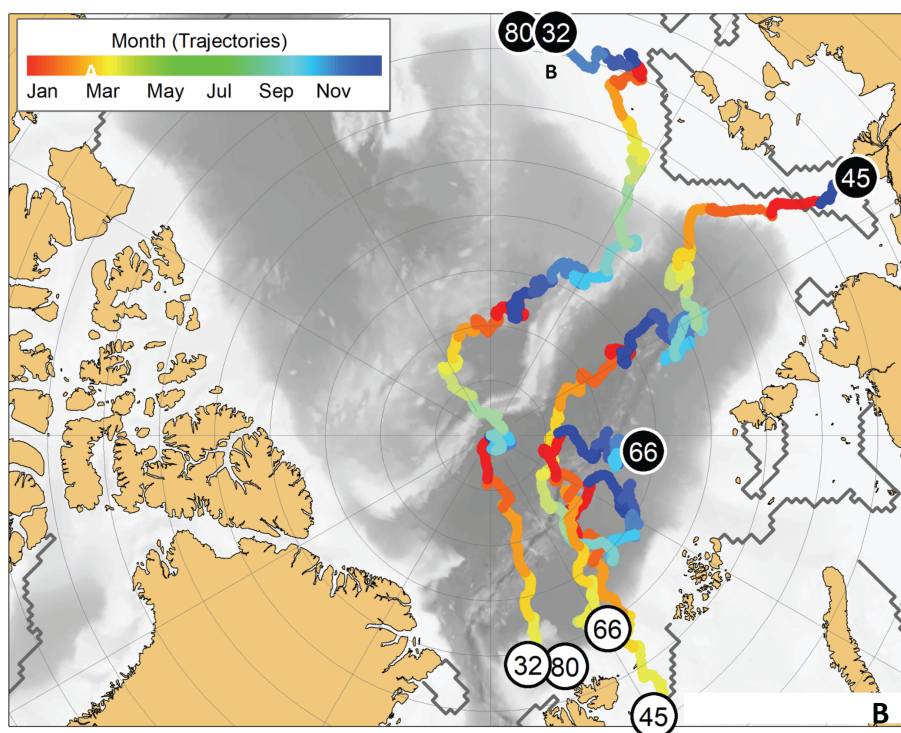
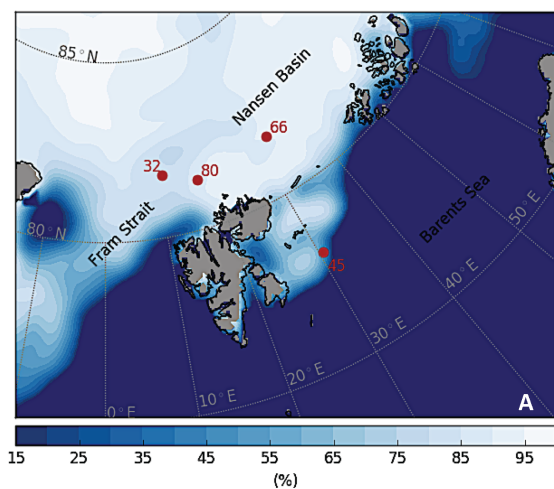
749 Tab. 3: Dissolution experiments on cryogenic gypsum crystals. ‘Water mass’ simulating
 750 experiments with 34.9% sterile filtered seawater. Each experiment was conducted in parallel
 751 in 3-4 separate pressure chambers.

752

753 **Figure captions:**

754

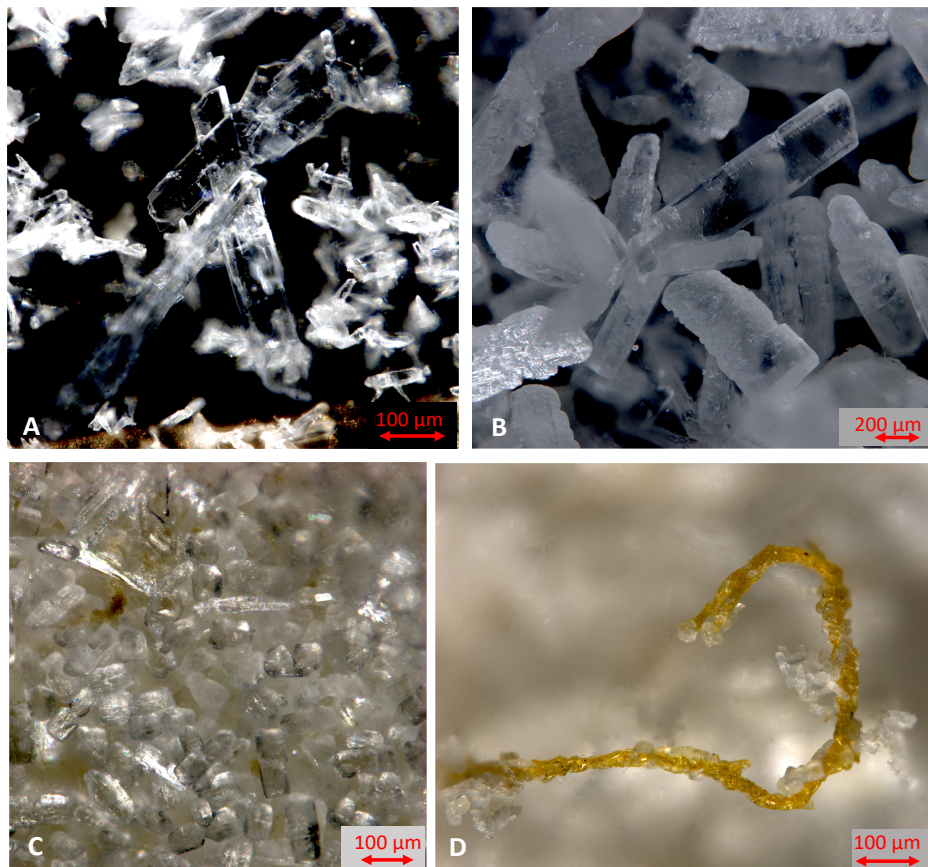
755



756
757 Fig. 1: Study area with sample locations. A: Sea ice coverage at the station and time of
758 sampling in %. B) Trajectories of the sea ice from which the cryogenic gypsum was released.
759 Each trajectory starts where sea ice formed (black circles), and shows its drift until the time

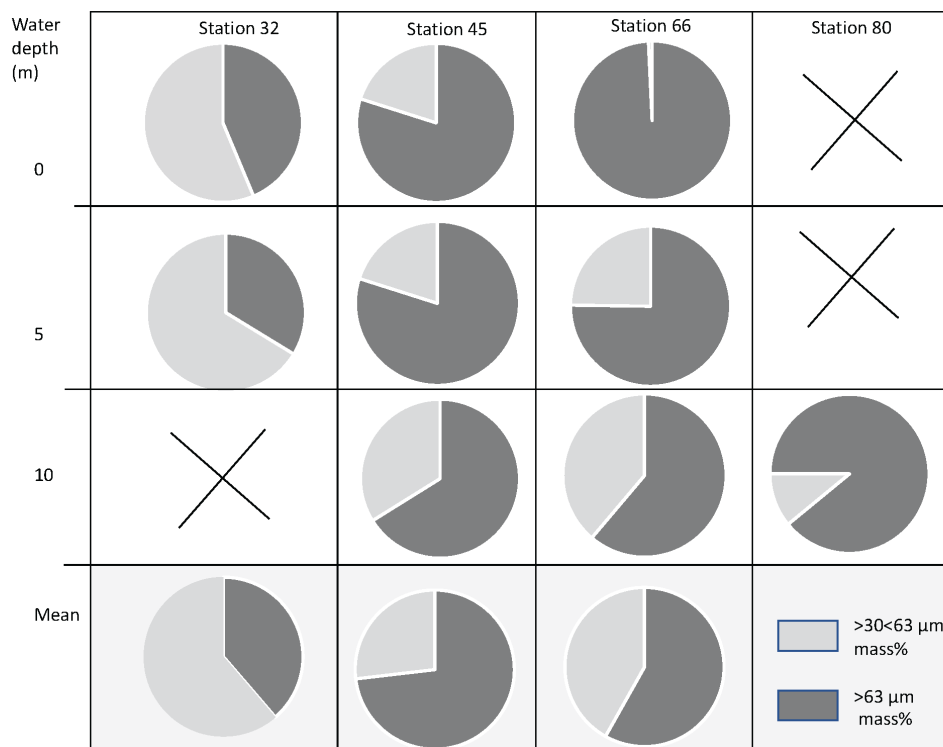


760 and place of sampling (white circles). The colour scale of the drift trajectories indicates the
761 month in which the back-tracked sea ice was at any given position.



762
763 Fig. 2: Cryogenic gypsum crystals collected during Polarstern expedition PS106-1 from the
764 upper water column. A) Crystals collected from station 66 at 5 m water depth. B) Crystals
765 collected from station 66 at 0 m water depths. C) Crystals collected from station 45 at 10 m
766 water depth. D) Crystals collected from station 45 at 10 m water depths entangled in an algae
767 filament.

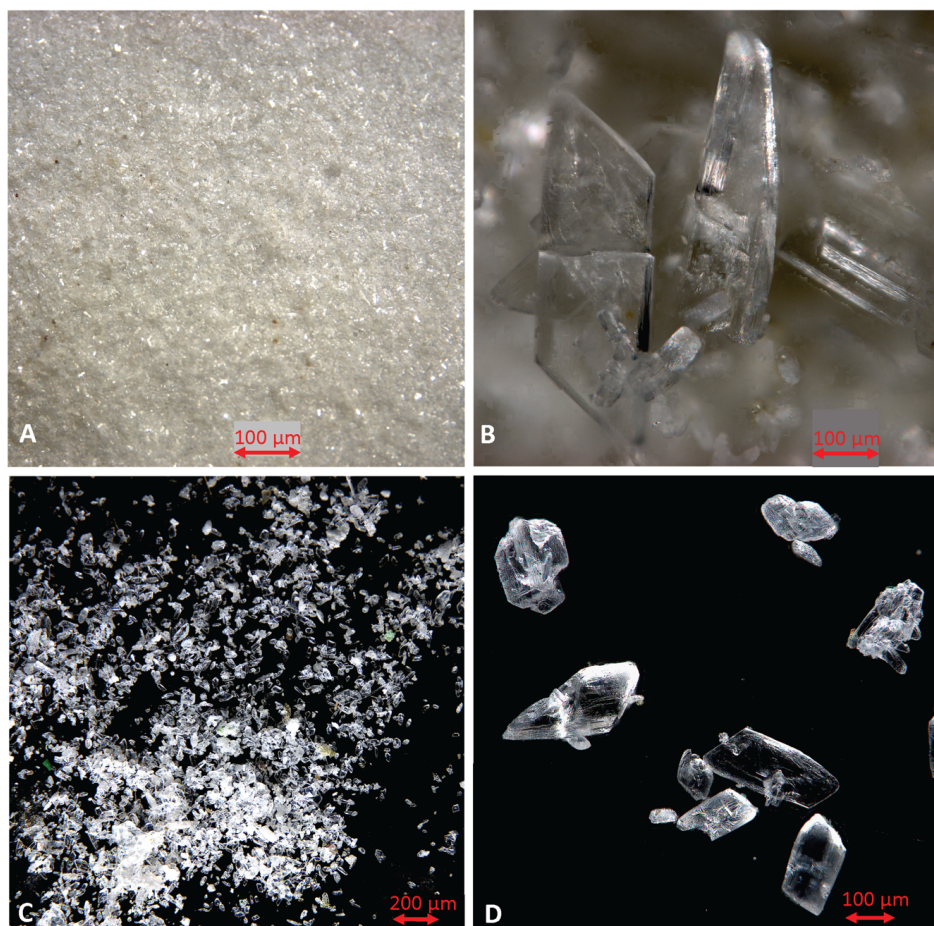
768
769
770



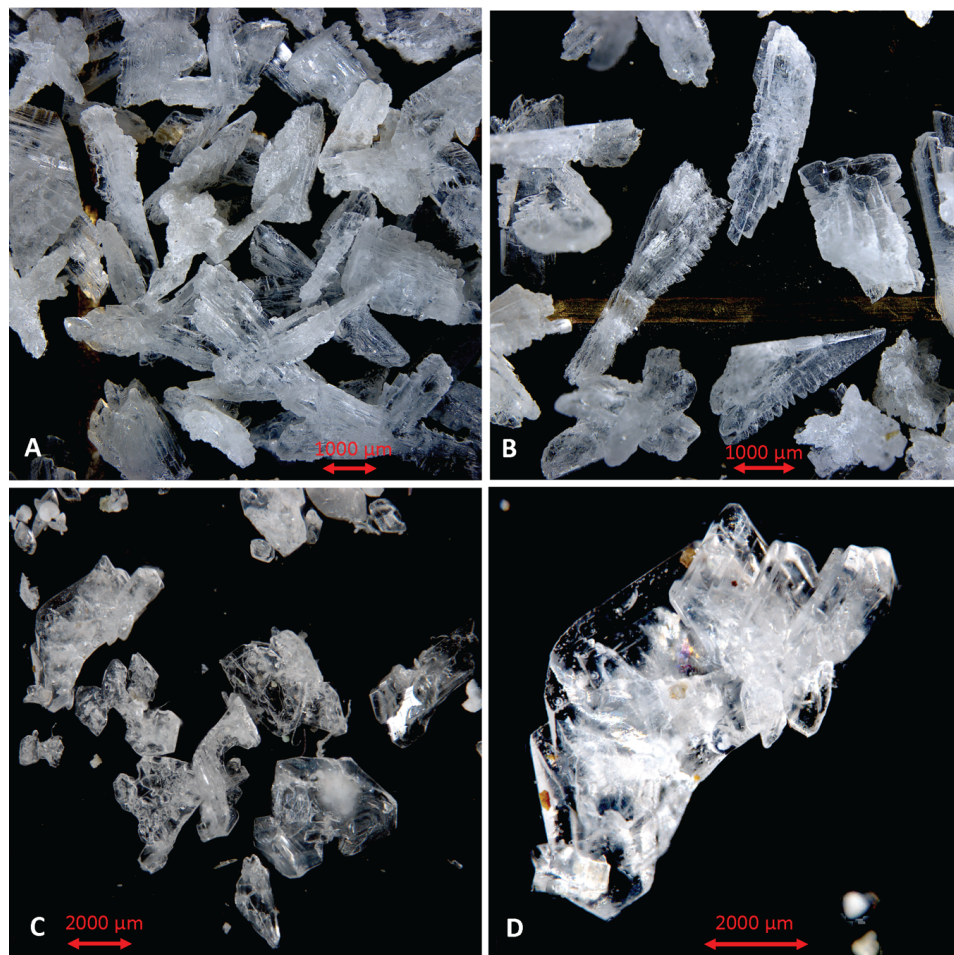
771

772 Fig. 3: Proportional mass (%) of cryogenic gypsum for the size fractions >30<63 μm and >63
773 μm for all ROV samples.

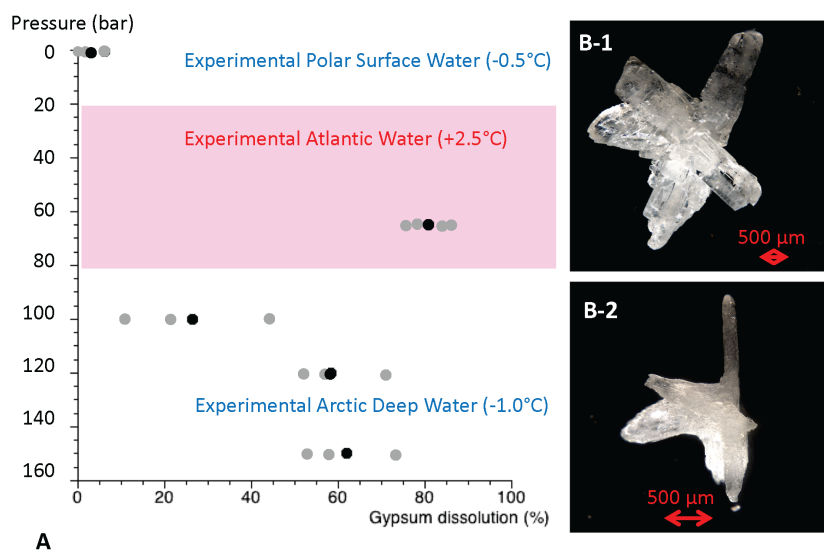
774



775
776 Fig. 4: Comparison of cryogenic gypsum crystals collected from the water column at station
777 PS45 (10 m water depth) (A-B) with crystals retrieved from an ice-core collected above the
778 ROVnet sampling area (C-D).
779
780



781
782 Fig. 5: Comparison of cryogenic gypsum crystals collected from the water column at station
783 PS80-2 (10 m water depth) (A-B) with crystals retrieved from an ice-core collected above the
784 ROVnet sampling area (C-D).
785
786

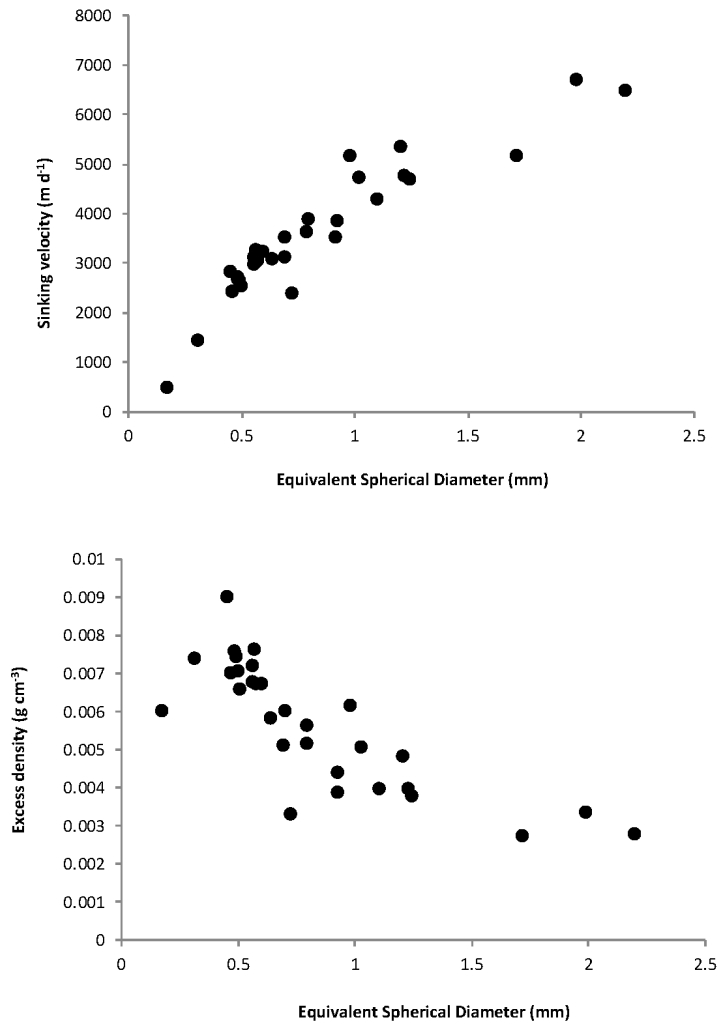


787

788 Figure 6: Results from cryogenic gypsum dissolution experiments. A) Graph showing the
789 position of the simulated Arctic water masses in respect to pressure and temperature and how
790 much gypsum (%) was dissolved on average over a 24-hours lasting exposure to such
791 pressure and temperature conditions. Grey dots indicate the values from each aquarium, black
792 dots the mean per experiment. B-1) Cryogenic gypsum crystal of the 120 bar-experiment
793 before exposure. B-2) The same cryogenic gypsum crystal of the 120 bar-experiment after 24
794 hours.

795

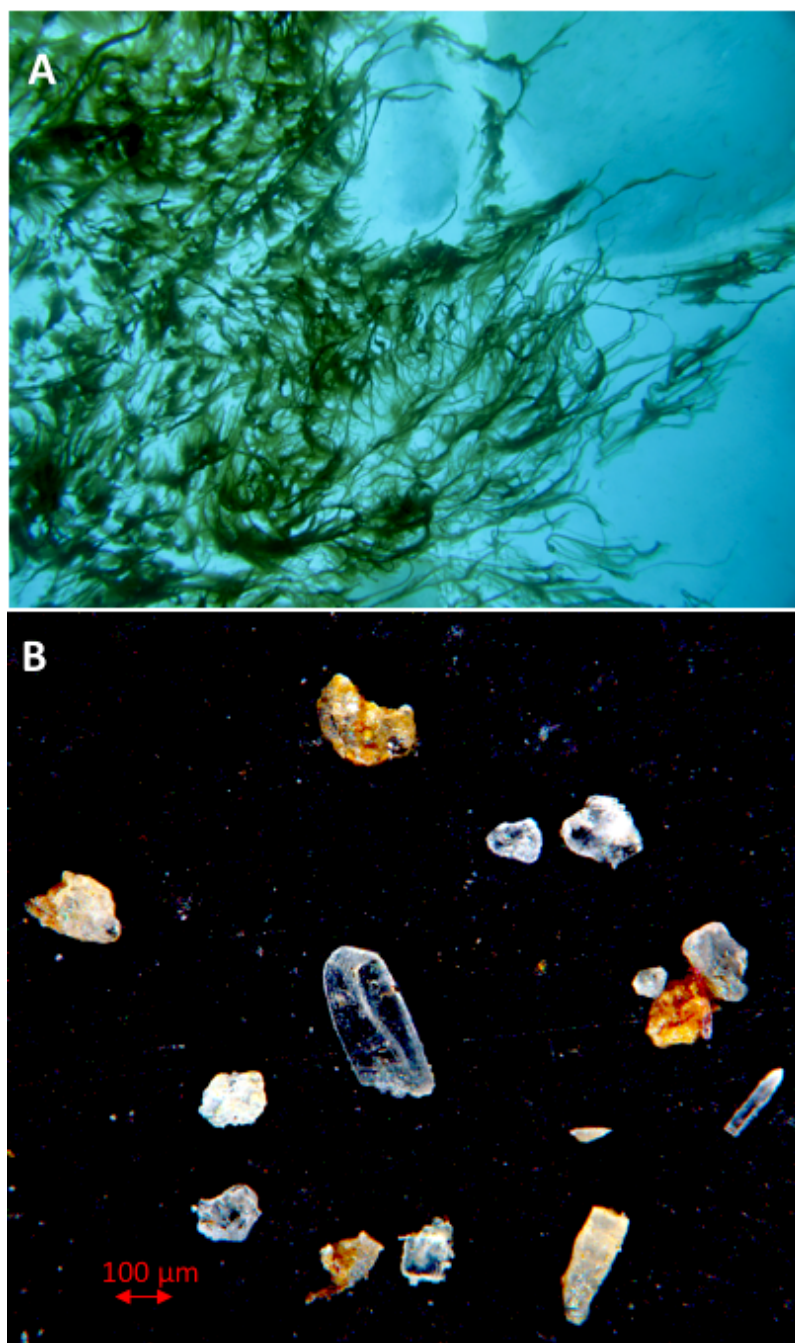
796



797

798 Fig. 7: (A) sinking velocity and (B) excess density (excess density = gypsum density –
799 seawater density) of cryogenic gypsum crystals plotted against equivalent spherical diameter
800 (ESD).

801



802
803 Fig. 8: Living *Melosira arctica* curtains hanging from ice flows during the PS106 expedition
804 (photo taken by M. Nicolaus and C. Katlein). Cryogenic gypsum isolated from *Melosira*
805 *arctica* (PS106-1, station 21 (Peeken, 2018)).
806



807

808 **Acknowledgement:**

809 We thank Gernot Nehrke for performing Raman Spectroscopy on crystals from all catches.
810 Christoph Vogt and Dieter Wolf-Gladrow made valuable comments on the manuscript and we
811 thank them very much for it. We thank the captain and crew of RV Polarstern expedition
812 PS106 for their support at sea. This study was funded by the PACES (Polar Regions and
813 Coasts in a Changing Earth System) Program of the Helmholtz Association, the Helmholtz
814 Infrastructure Fund “Frontiers in Arctic Marine Monitoring (FRAM)”. This study used
815 samples and data provided by the Alfred-Wegener-Institut Helmholtz-Zentrum für Polar- und
816 Meeresforschung in Bremerhaven from *Polarstern* expedition PS 106 (Grant No. AWI-
817 PS106_00).

818

819 **Author Contributions:**

820 J.W. lead the writing of this manuscript as well as gypsum sample preparation and analysis.
821 H.F., I.P., C.K., G.C., M.N. acquired ROVnet and ice samples in the field. M.I. measured
822 crystal settling velocities. T.K. performed the backtracking analysis. All authors contributed
823 to the writing and editing of the manuscript

824

825

826

827

828

829